PAPER • OPEN ACCESS

Poloidal structure of the edge parallel flow in H-mode, L-mode and I-mode confinement regimes

OPEN ACCESS
IOP Publishing | International Atomic Energy Agency
Nuclear Fusion
Nucl. Fusion **64** (2024) 076051 (7pp)
https://doi.org/10.1088/1741-4326/ad518f

Poloidal structure of the edge parallel flow in H-mode, L-mode and I-mode confinement regimes

D.J. Cruz-Zabala[1,*], E. Viezzer[1], P. Cano-Megias[2], M. Cavedon[3], R. Dux[2], U. Plank[2], T. Pütterich[2], K. McKay[1], A. Rodriguez-Gonzalez[1], M. Garcia-Munoz[1] and the ASDEX Upgrade Team[a]

[1] Department of Atomic, Molecular and Nuclear Physics, University of Seville, Seville, Spain
[2] Max-Planck-Institut für Plasmaphysik, Garching, Germany
[3] Dipartimento di Fisica 'G. Occhialini', Università di Milano-Bicocca, Milano, Italy

E-mail: dcruz3@us.es

Received 28 December 2023, revised 10 May 2024
Accepted for publication 29 May 2024
Published 12 June 2024

Abstract

Impurity profiles have been measured with the edge high field side (HFS) and low field side (LFS) charge exchange recombination spectroscopy suite at ASDEX Upgrade enabling the study of the poloidal structure of the edge parallel flow in H-mode, L-mode and I-mode. In H-mode, asymmetries in the impurity density, toroidal and poloidal rotations are found. In I-mode, only toroidal rotation asymmetries have been measured while in L-mode no asymmetries have been observed. The measured parallel flow can be divided in two components, the Pfirsch–Schlüter (PS) flow and the symmetric flow. Two different methods have been followed to determine both contributions to the parallel flow. The first method is based on the calculation of the PS flow at the HFS and LFS from the radial electric field. The second method directly provides the symmetric flow from the flux surface average (FSA) of the parallel flow. In H-mode, the methods provide different results, while in L-mode and I-mode they agree. The differences observed in H-mode between the two methods could be explained by the existence of asymmetries in the impurity density, by the non-negligible particle sources and radial losses, or by the approximations made in the calculation of the FSA of the parallel flow from measurements in two poloidal positions (midplane HFS and LFS) only.

Keywords: impurity, asymmetry, CXRS, flows

(Some figures may appear in colour only in the online journal)

[a] See Zohm *et al* 2024 (https://doi.org/10.1088/1741-4326/ad249d) for the ASDEX Upgrade Team.
[*] Author to whom any correspondence should be addressed.

1. Introduction

Plasma rotation will play a major role in future fusion devices as it is one of the key elements for the suppression of different plasma instabilities [1–7]. The nature of the edge flow, and how it couples to the plasma core, is important for accurately modelling the rotation profile in present and future devices from first principles. Furthermore, plasma rotation is one of the ingredients of particle transport, which governs the confinement of the plasma. In particular, understanding the impurity transport is mandatory to prevent fuel dilution and disruptions in future fusion devices. Impurities are also important for diagnosing the plasma, as, compared to main ions, these species can be measured more easily [8]. The most common technique to obtain the impurity rotation, temperature and density is Charge eXchange Recombination Spectroscopy (CXRS) [9]. It is based on the charge transfer between injected neutral atoms (D) and ionized impurities (A^{Z+}) that are present in the plasma:

$$A^{Z^+} + D \rightarrow A^{(Z-1)^{+*}} + D^+ \rightarrow A^{(Z-1)^+} + D^+ + h\nu.$$

After the charge transfer, the impurities emit light, which is analysed with a spectrometer. The Doppler width and shift are related to the temperature and rotation, respectively, while the intensity of the signal is proportional to the impurity density. The CXRS technique provides measurements at specific positions in the plasma, normally at the Low Field Side (LFS). However, previous studies have shown that the impurity properties vary poloidally [10–17]. Hence, to fully understand the poloidal impurity distribution, measurements at different poloidal positions are desirable. At ASDEX Upgrade (AUG), a gas puff based CXRS diagnostic measures at the High Field Side (HFS) midplane edge [18] which, combined with the edge LFS suite of CXRS diagnostics [19, 20], enable edge impurity asymmetry studies between LFS and HFS.

This work is focussed on the study of the poloidal structure of the edge parallel flow in different confinement regimes. In neoclassical theory, the parallel flow can be divided in two contributions: the Pfirsch–Schlüter (PS) flow and the symmetric flow. The PS flow is a parallel flow that compensates the charge separation produced by the perpendicular flow while the symmetric flow is a consequence of the particle continuity equation, as will be shown later in section 2. Two methods are used to calculate both contributions: one is based on the radial electric field and the other on the flux surface average (FSA) of the total parallel flow. The methodology followed to determine the two contributions to the parallel flow is described in section 2. To experimentally address this, edge HFS and LFS CXRS measurements are presented in H-mode [21], L-mode and I-mode [22, 23]. These measurements are described in section 3 and they allow us to obtain the two contributions to the parallel flow. In section 4, it is shown how the use of two different methods to experimentally obtain the two contributions of the parallel flow allow us to explore the limits of neoclassical theory. A summary and an outlook are given in section 5.

2. Determination of the parallel velocity components

The neoclassical expressions for the parallel and perpendicular velocities applied in this work follow the reasoning described in [11], which is based on [10]. The important equations needed to properly discuss the results shown in section 4 are derived again here. The conservation of the particle flux is described by the particle continuity equation:

$$\frac{\partial n_\alpha}{\partial t} + \nabla \cdot (n_\alpha \mathbf{v}_\alpha) = S \tag{1}$$

where n_α and $\mathbf{v}_\alpha$ are the density and the total velocity of the species α, respectively, and S accounts for particle sources and sinks. The studies carried out here are not transient and no sources are considered. This reduces equation (1) to:

$$\nabla \cdot (n_\alpha \mathbf{v}_\alpha) = 0. \tag{2}$$

In neoclassical theory it is assumed that the impurity density is a flux function, which means that the 3D flow has to be divergence free. In the following, the divergence of the radial flow is considered to be negligible and the structure of the flow on a flux surface is studied. The 2D divergence free flow can be expressed as:

$$\mathbf{v}_\alpha = \omega_\alpha(\psi) R\mathbf{e}_\phi + K_\alpha(\psi) B\mathbf{e}_\parallel \tag{3}$$

where R is the major radius, ψ is the poloidal magnetic flux and $\omega_\alpha(\psi)$ and $K_\alpha(\psi)$ are considered to be flux functions, which means that they take the same value for every point contained in a given flux surface. $\omega_\alpha(\psi)$ is identified as the angular frequency of a toroidal rigid body rotator and is given by:

$$\omega_\alpha(\psi) = -\frac{\partial \Phi(\psi)}{\partial \psi} - \frac{1}{q_\alpha n_\alpha(\psi)} \frac{\partial p_\alpha(\psi)}{\partial \psi} \tag{4}$$

with $\Phi(\psi)$ being the electrostatic potential and q_α and $p_\alpha(\psi)$ the charge and the pressure of the species α, respectively. Note that $n_\alpha(\psi)$, $\Phi(\psi)$ and $p_\alpha(\psi)$ are considered to be flux functions. The flux function $K_\alpha(\psi)$ accounts for a degree of freedom given by the fact that any term proportional to the magnetic field $\mathbf{B}$ is also divergence free as $\nabla \cdot \mathbf{B} = 0$. From equation (3), expressions for the perpendicular ($\perp$) and parallel ($\parallel$) velocities can be derived:

$$\mathbf{v}_{\perp,\alpha} = \omega_\alpha(\psi) \frac{RB_\theta}{B} \mathbf{e}_\perp \tag{5}$$

$$\mathbf{v}_{\parallel,\alpha} = \omega_\alpha(\psi) \frac{RB_\phi}{B} \mathbf{e}_\parallel + K_\alpha(\psi) B\mathbf{e}_\parallel \tag{6}$$

where $\mathbf{e}_\phi = \frac{B_\phi}{B}\mathbf{e}_\parallel + \frac{B_\theta}{B}\mathbf{e}_\perp$ has been used. Knowing that $\mathbf{e}_\perp = -\frac{B_\phi}{B}\mathbf{e}_\theta + \frac{B_\theta}{B}\mathbf{e}_\phi$ and $\mathbf{e}_\theta = -\frac{B_\phi}{B}\mathbf{e}_\perp + \frac{B_\theta}{B}\mathbf{e}_\parallel$ with ϕ representing the toroidal direction and θ the poloidal direction, equation (5) becomes:

$$\mathbf{v}_{\perp,\alpha} = \omega_\alpha(\psi) \left(-\frac{RB_\phi}{B} \mathbf{e}_\parallel + R\mathbf{e}_\phi \right). \tag{7}$$

The first terms of equations (6) and (7) only differ in the sign and are not divergence free as $\nabla\cdot(\frac{1}{B}\mathbf{e}_\parallel)\neq 0$. However, when summing both equations to obtain the total velocity $\mathbf{v}_\alpha$, these terms cancel each other. The remaining terms are divergence free as $\nabla\cdot(B\mathbf{e}_\parallel)=0$ and $\nabla\cdot(R\mathbf{e}_\phi)=0$. Considering now the particular case of $K_\alpha(\psi)=-\omega_\alpha(\psi)\frac{RB_\phi}{\langle B^2\rangle}+\frac{u_\alpha}{\langle B^2\rangle}$, equation (6) can be rewritten in the following way:

$$\mathbf{v}_{\parallel,\alpha}=\omega_\alpha(\psi)RB_\phi\left(\frac{1}{B}-\frac{B}{\langle B^2\rangle}\right)\mathbf{e}_\parallel+u_\alpha\frac{B}{\langle B^2\rangle}\mathbf{e}_\parallel \tag{8}$$

where $\langle\ldots\rangle$ defines the FSA and u_α is defined as $u_\alpha=\langle\mathbf{v}_\parallel\mathbf{B}\rangle$, which is of interest for future calculations (see section 2.2). The second term of equation (8) is the symmetric flow while the first term is the PS flow:

$$v_{PS,\alpha}\mathbf{e}_\parallel=\omega_\alpha(\psi)RB_\phi\left(\frac{1}{B}-\frac{B}{\langle B^2\rangle}\right)\mathbf{e}_\parallel. \tag{9}$$

The structure of the PS flow is different between HFS and LFS due to the change of sign at the radial position that satisfies $B^2=\langle B^2\rangle$.

The objective of this work is to experimentally determine the two components of equation (8) following two different methods. These two methods are described in detail in [24, 25] and are applied here to tokamak plasmas. The agreement or disagreement between the methods will be analysed for the H-mode, L-mode and I-mode plasmas described in section 3 and conclusions will be extracted.

2.1. Method based on the radial electric field E_r

The radial electric field E_r can be calculated using the radial force balance equation:

$$E_r=\frac{1}{n_\alpha(\psi)q_\alpha}\frac{\partial p_\alpha(\psi)}{\partial r}-v_{\theta,\alpha}B_\phi+v_{\phi,\alpha}B_\theta \tag{10}$$

where r is the minor radius. The PS flows at the LFS and at the HFS are derived from $\omega_\alpha(\psi)=(E_r-\frac{1}{q_\alpha n_\alpha(\psi)}\frac{\partial p_\alpha(\psi)}{\partial r})\frac{1}{RB_\theta}$ using:

$$v_{\mathrm{PS}}^L=(\omega_\alpha(\psi)RB_\phi)^L\left(\frac{1}{B}-\frac{B}{\langle B^2\rangle}\right)^L \tag{11}$$

$$v_{\mathrm{PS}}^H=(\omega_\alpha(\psi)RB_\phi)^L\left(\frac{1}{B}-\frac{B}{\langle B^2\rangle}\right)^H \tag{12}$$

where the superscripts L and H stand for LFS and HFS, respectively. Note that this method assumes that $\omega(\psi)$ is a flux function and, then, the differences between v_{PS}^L and v_{PS}^H come only from the factor $\left(\frac{1}{B}-\frac{B}{\langle B^2\rangle}\right)$, as RB_ϕ is a constant. Once the PS flows are calculated, u_α is obtained following equation (8):

$$u_\alpha=\left[\left(v_\parallel-v_{\mathrm{PS}}\right)\frac{1}{B}\right]^L\langle B^2\rangle. \tag{13}$$

2.2. Method based on the FSA of the parallel flow

This method takes advantage of the fact that:

$$u_\alpha=\langle\mathbf{v}_\parallel\mathbf{B}\rangle \tag{14}$$

which means that u_α can be directly obtained from the FSA of the parallel flow and the magnetic field. This FSA can be calculated from the LFS and HFS measurements. Note that the FSA can be understood as an average over the poloidal direction. In this case, it is considered that the full poloidal plane can be described by the HFS and LFS midplane profiles. This is an approximation as the parallel rotation could vary dramatically between HFS and LFS. Taking this into account, the PS flows at the LFS and HFS can be calculated following equations (8) and (9) as:

$$v_{\mathrm{PS}}^L=v_\parallel^L-u_\alpha\frac{B^L}{\langle B^2\rangle} \tag{15}$$

$$v_{\mathrm{PS}}^H=v_\parallel^H-u_\alpha\frac{B^H}{\langle B^2\rangle}. \tag{16}$$

In summary, the first method uses the experimental measurements to calculate the PS flows at the HFS and LFS and applies equation (8) to determine u_α, while the second method takes advantage of having measurements at two poloidal positions to compute u_α from a FSA (equation (14)) and the PS flows are determined using equation (8). The difference between the methods is which term from equation (8) is determined from experimental measurements and which one is determined imposing equation (8), considering that the total parallel flow $\mathbf{v}_{\parallel,\alpha}$ is known at the LFS and HFS. If the assumptions made are correct the methods should agree.

3. Edge impurity asymmetries in H-mode, L-mode and I-mode

In this section, the measured LFS and HFS edge impurity profiles are discussed. Figure 1 shows the impurity temperature (upper row), toroidal rotation (middle row) and poloidal rotation (lower row) obtained in H-mode (left column), L-mode (middle column) and I-mode (right column) plasmas. Both plasma discharges, #37529 (H-mode) and #38905 (L-mode and I-mode) were operated with a toroidal magnetic field of -2.5 T and a plasma current of 1.0 MA. Note that the H-mode discharge was performed in lower single null with favourable ∇B drift while the discharge with L-mode and I-mode phases was executed in upper single null with unfavourable ∇B drift. LFS and HFS measurements are taken at different radial positions but they are mapped to the normalized poloidal magnetic flux coordinate ρ_{pol}.

The H-mode profiles (left column of figure 1) correspond to the profiles discussed in [17]. They are shown here with the purpose of studying the poloidal structure of the parallel flow and to compare to the L-mode and I-mode cases. In H-mode, asymmetries in both the poloidal ($v_{\theta,\alpha}$) and the toroidal ($v_{\phi,\alpha}$) impurity rotations are observed while the impurity temperature (T_α) is poloidally symmetric [10, 11, 14, 17]. The toroidal

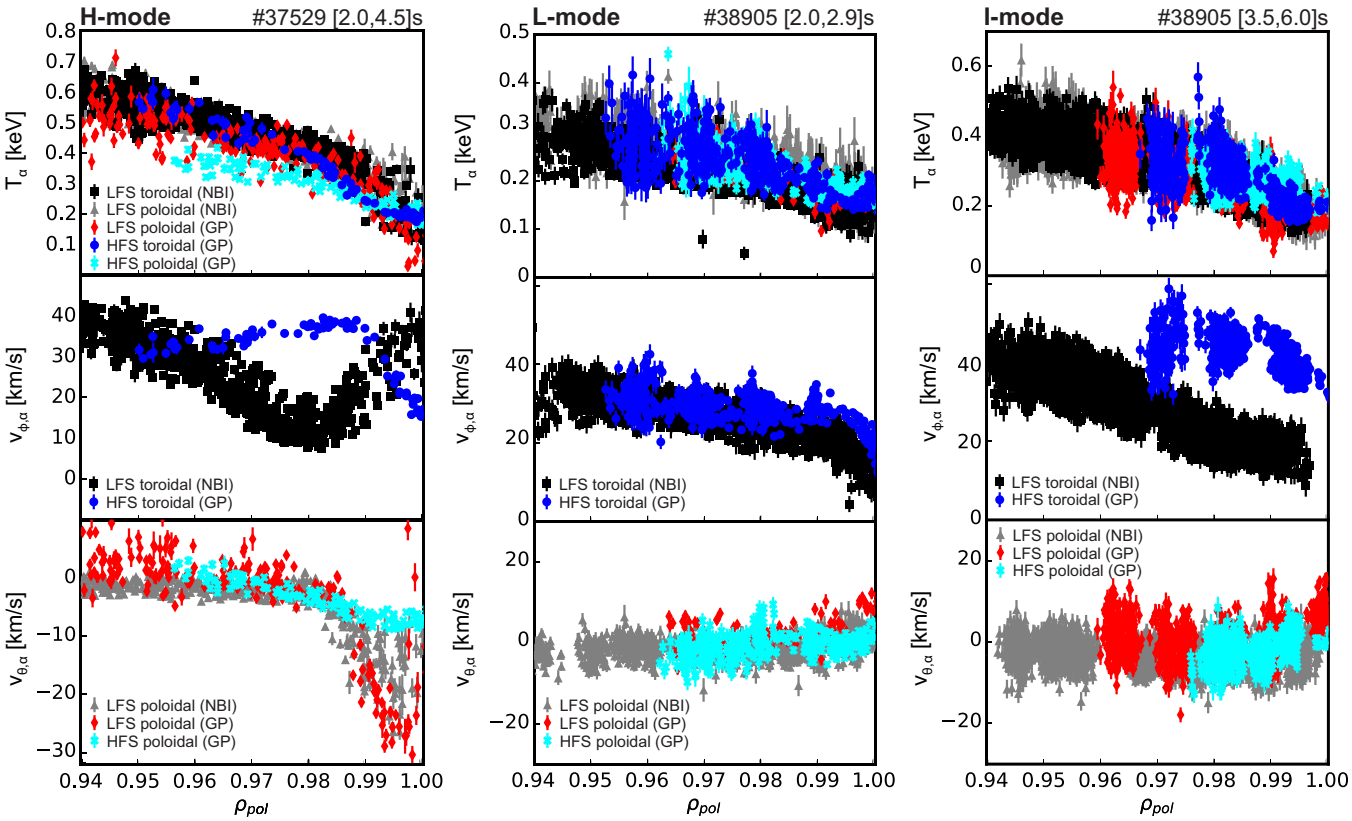

Figure 1. Impurity temperature (upper row), toroidal rotation (middle row) and poloidal rotation (lower row) of H-mode (left column), L-mode (middle column) and I-mode (right column) plasmas. (left) Adapted from [17]. © IOP Publishing Ltd. All rights reserved.

rotation shows a different shape at the HFS compared to the LFS. While it shows a minimum close to the separatrix at the LFS, a maximum is observed at the HFS. At both poloidal locations, the toroidal rotation is co-current. The poloidal impurity rotation is close to zero towards the plasma core at both the LFS and HFS, but towards the separatrix, it increases in magnitude at both locations. However, it is larger in magnitude at the LFS compared to the HFS. Even if the magnitudes are different between HFS and LFS, both go in the electron diamagnetic direction (poloidally upwards at the LFS and downwards at the HFS). Note that, due to the different magnetic field strengths between HFS and LFS, different poloidal velocities between these regions are expected. However, the differences between the HFS and LFS poloidal velocities are larger than the expected changes due to the different HFS and LFS magnetic fields. This implies that impurity density asymmetries exist. The asymmetry factor, which is defined as the ratio between HFS and LFS impurity densities, can be estimated from [10, 11, 17]:

$$\frac{n_\alpha^H}{n_\alpha^L} \approx \frac{v_{\theta,\alpha}^L B_\theta^H}{v_{\theta,\alpha}^H B_\theta^L}. \tag{17}$$

This particular plasma was analysed in detail in [17] it was found that the edge HFS impurity density was up to three times larger compared to the edge LFS impurity density. The asymmetry factors obtained from the ratio between the impurity densities and using equation (17) matched well.

In L-mode and I-mode (see middle and right column of figure 1, respectively) good agreement is observed in the impurity temperature measured with the different diagnostics. Note the different temperature scales between both regimes. As the injected power is increased during the I-mode, the temperature is higher in this phase. Different behaviours are observed in the toroidal impurity rotation between the two regimes. The L-mode regime is the only regime where no clear poloidal asymmetry is found in the toroidal impurity rotation. In I-mode, toroidal impurity velocity asymmetries, similar to the ones found in H-mode (see left column of figure 1), are measured with the difference that, in I-mode, no clear minimum is observed in the LFS toroidal velocity. The poloidal impurity velocity behaves similarly in L-mode and I-mode. It is close to zero at both the LFS and HFS with a slight increase towards the separatrix. Taking into account equation (17) and considering that the poloidal rotations are similar at the HFS and LFS, no poloidal impurity density asymmetries are expected in L-mode and I-mode. Note that the ratio of poloidal magnetic fields between HFS and LFS is close to one ($B_\theta^H/B_\theta^L \approx 1.2$–$1.3$) in this discharge. Unfortunately, no impurity density measurements are available at the HFS in this specific discharge. However, as commented for the H-mode case, equation (17) should describe accurately the asymmetry factor. The absence of impurity density asymmetries in L-mode and I-mode is in agreement with observations at Alcator C-Mod [26]. In summary, no asymmetries in the impurity temperature, toroidal rotation, poloidal rotation and density are

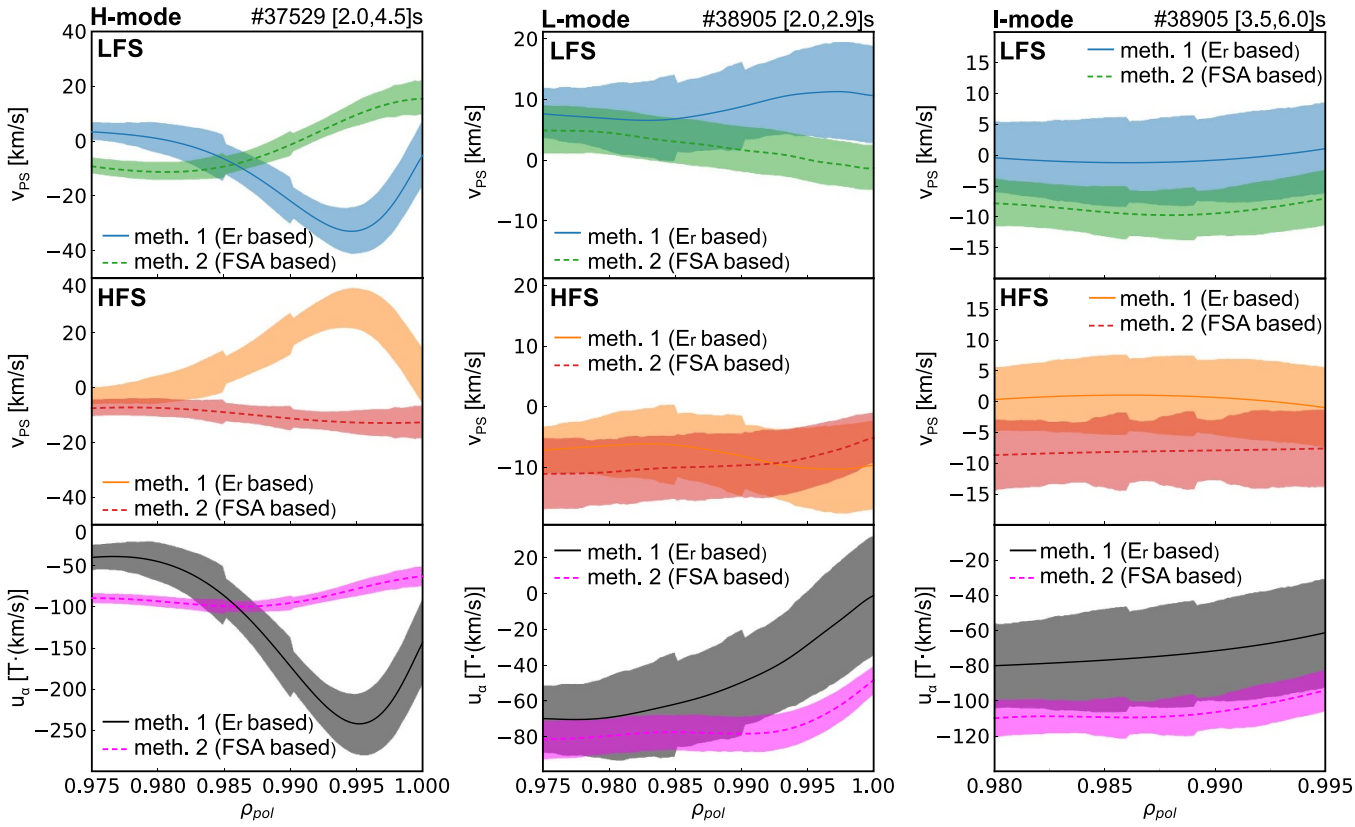

Figure 2. PS flow at the LFS (upper row), at the HFS (middle row) and u_α constant (lower row) in H-mode (left column), L-mode (middle column) and I-mode (right column) obtained with the described methods.

found in L-mode. In I-mode, only toroidal impurity rotation asymmetries are found.

4. The parallel flow structure in H-mode, L-mode and I-mode

Figure 2 shows the PS flow at the LFS (upper row), at the HFS (middle row) and the FSA u_α (lower row) in H-mode (left column), L-mode (middle column) and I-mode (right column) obtained with the two methods described in section 2.

In H-mode, the methods provide different results, especially in the region where the impurity density asymmetry exists ($0.985 < \rho_{\rm pol} < 1.000$ in this particular discharge according to [17]). Note that the equations derived in section 2 assume that the impurity density is a flux function, which is not the case here. Note also that the second method calculates the FSA $u_\alpha = \langle \mathbf{v}_{\|}\mathbf{B}\rangle$ from only two poloidal positions (LFS and HFS). This implies that the poloidal dependence of the parallel rotation in regions which are not the HFS midplane and LFS midplane are neglected. In order to calculate this FSA in a more accurate way, measurements of the impurity flows in more poloidal positions would be required.

The L-mode (middle column) and I-mode (right column) calculations show good agreement between the methods, contrary to the H-mode case. Please note the different radial ranges analysed in L-mode and I-mode due to the reduced radial range with experimental data in the I-mode case (see figure 1). As a consequence of the different vertical axes of figure 2, the error bars of the L-mode and I-mode cases seem to be bigger than the ones of the H-mode case, but they are similar or even smaller depending on the radial position. The major differences between the two methods are found in the outer part of the LFS L-mode calculations. However, even if in this specific region the methods do not match within the uncertainties, both curves are close and follow the same trend.

The agreement between the methods in L-mode and I-mode supports the idea that the impurity density asymmetries might be playing a role in the differences found in H-mode. In L-mode and I-mode, no impurity density asymmetries are found and the methods provide the same results. Note, however, that the second method does not provide a change of sign between the PS flow at the HFS and at the LFS in the I-mode case. This might be related to the fact that the FSA $u_\alpha = \langle \mathbf{v}_{\|}\mathbf{B}\rangle$ is calculated considering only two poloidal positions (HFS and LFS midplanes). Note also the larger contribution of the PS flow in the H-mode case compared to the L-mode and I-mode cases. This is related to the fact that the edge transport barrier (ETB) developed in H-mode is reflected in a larger impurity poloidal velocity at the edge (see figure 1), which is one of the contributions to the PS flow. This bigger contribution to the PS flow due to the ETB in H-mode might be responsible for the differences observed between the two methods in this regime. In H-mode, the ETB is linked to a large E_r well [27] which implies a large edge impurity poloidal velocity at the LFS (see figure 1). At

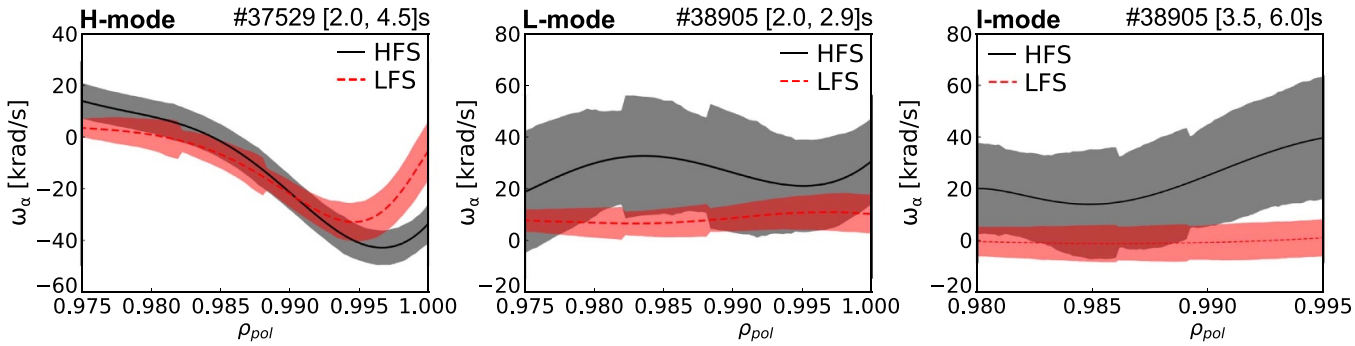

Figure 3. ω_α at the LFS and HFS in H-mode (left), L-mode (middle) and I-mode (right).

the HFS, the edge impurity poloidal velocity is much smaller in absolute value which, according to equation (17), means that edge impurity density asymmetries exist [17]. In L-mode and I-mode, no ETB and no impurity density asymmetries exist, so the two methods coincide. The existence of an ETB might be linked to the disagreement between the two methods observed in H-mode.

The procedure followed in section 2, which is based on neoclassical theory, assumes that ω_α is a flux function and it uses its value at the LFS to obtain $v_{\rm PS}^L$ and $v_{\rm PS}^H$. It is, therefore, important to check whether this assumption might be responsible for the different behaviours observed between H-mode and L/I-modes. Figure 3 shows ω_α at the LFS and HFS for the three regimes. It can be seen that they agree in almost the whole radial range analysed for the three regimes, so we can conclude that the assumption of ω_α being a flux function can not explain the agreement or disagreement between the two methods. Note that the behaviours shown in figure 2 do not change if ω_α^H is used to calculate $v_{\rm PS}^H$ in equation (12) instead of ω_α^L.

Several explanations can describe the discrepancies observed between the two methods in H-mode. The first is that the presence of impurity density asymmetries can affect the parallel velocity. These impurity density asymmetries might be linked to the existence of an ETB, as mentioned above. This explanation is in agreement with the fact that in L-mode and I-mode no impurity density asymmetry exist and the methods coincide. The second possible explanation could be that impurity sources and radial flows might not be negligible [28] . This assumption was made to get equation (3) from equation (1). The third possible explanation is that the method based on the FSA of the parallel flow is simplifying the poloidal dependence of the parallel flow as it is only considering HFS and LFS midplane profiles to evaluate the FSA. If the first or (and) the second explanation(s) is (are) true, it might be an indication of the limitations of neoclassical theory at the very edge of the plasma. If the third explanation is correct, the discrepancies between the methods would come from the inaccuracy of the FSA calculation and neoclassical theory might still be applicable in this region of the plasma.

To answer the question of which method is best suited to calculate the components of the parallel flow, the results of the L-mode and I-mode cases are considered. Even if in these two regimes, the methods agree within the uncertainties, the method based on the FSA of the parallel velocities does not provide a change of sign between the PS flow at the HFS and LFS. This might be due to the fact that the poloidal dependence of the parallel flow is approximated using only midplane HFS and LFS profiles, as explained above. According to this, the method based on the E_r profile is more accurate when only few measurement positions are available along the poloidal plane.

5. Summary and outlook

The poloidal structure of the parallel flow has been studied using the HFS edge CXRS diagnostic [18] and the LFS edge CXRS suite [19, 20] at AUG. Dedicated experiments have been performed in H-mode, L-mode and I-mode. Two different methods have been employed to determine the two components of the parallel flow: the PS flow and the symmetric flow. The first method is based on the calculation of the PS flow at the HFS and LFS from the radial electric field. Then, the FSA u_α is calculated using the general expression of the parallel velocity. The second method calculates the symmetric flow computing the FSA of the parallel flow using the HFS and LFS measured velocities. Once the symmetric flow is known, the PS flows at the HFS and LFS are calculated using the general expression for the parallel velocities.

In H-mode, where edge asymmetries in the impurity density, toroidal and poloidal rotations are present, the methods provide different results. These differences are enhanced in the region where impurity density asymmetries exist. In L-mode and I-mode, the methods agree within the uncertainties. Note that no edge impurity density asymmetries are measured in L-mode and I-mode. It can be concluded that L-mode and I-mode are more similar in terms of particle transport compared to H-mode.

Three effects could explain the discrepancies between the two methods found in H-mode. The first one is that impurity density asymmetries break neoclassical theory at the edge affecting the parallel flow. This is in agreement with the fact that discrepancies are found in H-mode but not in L-mode and I-mode. The second possible explanation is that impurity sources and radial flows can not be neglected in the derivation of the parallel flow expression. The third

explanation supports the idea that the second method is inaccurate as it is simplifying the calculation of the FSA of the parallel flow using experimental measurements from HFS and LFS midplanes only. The fact that, in I-mode, the second method does not provide a change of sign in the PS flow between HFS and LFS supports this explanation. To shed more light on the details of this study, measurements in more poloidal positions are desirable.

Acknowledgments

Support from the project 'Impact of the shear flow on particle transport in confined fusion plasmas' PID2020-116822RB-I00 financed by the Ministry of Science, Innovation and Universities (MICIU/AEI /10.13039/501100011033) is gratefully acknowledged.

The support from the European Research Council (ERC) under the European Union's Horizon 2020 research and innovation programme (Grant Agreement No. 805162) is gratefully acknowledged.

ORCID iDs

D.J. Cruz-Zabala https://orcid.org/0000-0001-5925-5153
E. Viezzer https://orcid.org/0000-0001-6419-6848
P. Cano-Megias https://orcid.org/0000-0001-5182-6513
M. Cavedon https://orcid.org/0000-0002-0013-9753
R. Dux https://orcid.org/0000-0002-3447-9553
U. Plank https://orcid.org/0000-0002-1509-4308
T. Pütterich https://orcid.org/0000-0002-8487-4973
K. McKay https://orcid.org/0009-0005-1975-7673
A. Rodriguez-Gonzalez https://orcid.org/0000-0002-9284-3798
M. Garcia-Munoz https://orcid.org/0000-0002-3241-502X

References

[1] Hahm T.S. and Burrell K.H. 1995 *Phys. Plasmas* **2** 1648
[2] Burrell K.H. 1997 *Phys. Plasmas* **4** 1499–518
[3] Biglari H., Diamond P.H. and Terry P.W. 1990 *Phys. Fluids* B **2** 1–4
[4] Reimerdes H. *et al* 2007 *Phys. Rev. Lett.* **98** 055001
[5] Berkery J.W. *et al* 2010 *Phys. Rev. Lett.* **104** 035003
[6] Politzer P.A. *et al* 2008 *Nucl. Fusion* **48** 075001
[7] Garofalo A.M. *et al* 2002 *Phys. Rev. Lett.* **89** 235001
[8] Cano-Megias P. *et al* 2019 *J. Instrum.* **14** C10040
[9] Fonck R.J., Darrow D.S. and Jaehnig K.P. 1984 *Phys. Rev.* A **29** 3288–309
[10] Marr K.D. *et al* 2010 *Plasma Phys. Control. Fusion* **52** 055010
[11] Pütterich T. *et al* 2012 *Nucl. Fusion* **52** 083013
[12] Reinke M.L. *et al* 2012 *Plasma Phys. Control. Fusion* **54** 045004
[13] Reinke M.L. *et al* 2013 *Phys. Plasmas* **20** 056109
[14] Viezzer E. *et al* 2013 *Plasma Phys. Control. Fusion* **55** 124037
[15] Theiler C. *et al* 2014 *Nucl. Fusion* **54** 083017
[16] Churchill R.M. *et al* 2015 *Phys. Plasmas* **22** 056104
[17] Cruz-Zabala D.J. *et al* (the ASDEX Upgrade Team) 2022 *Plasma Phys. Control. Fusion* **64** 045021
[18] Cruz-Zabala D.J. *et al* 2019 *J. Instrum.* **14** C11006
[19] Viezzer E. *et al* 2012 *Rev. Sci. Instrum.* **83** 103501
[20] Plank U. 2022 The effect of the radial electric field around the separatrix on the access to the high confinement mode at ASDEX upgrade *PhD Dissertation* LMU München (https://doi.org/10.5282/edoc.29595)
[21] Wagner F. *et al* 1982 *Phys. Rev. Lett.* **49** 1408
[22] Whyte D.G. *et al* 2010 *Nucl. Fusion* **50** 105005
[23] Happel T. *et al* (the ASDEX Upgrade Team) 2016 *Plasma Phys. Control. Fusion* **59** 014004
[24] Chen J. *et al* 2019 *Nucl. Fusion* **59** 106036
[25] Yamamoto Y. *et al* 2020 *Phys. Plasmas* **27** 042514
[26] Churchill R.M., Lipschultz B. and Theiler C. 2013 *Nucl. Fusion* **53** 122002
[27] Viezzer E. *et al* 2013 *Nucl. Fusion* **53** 053005
[28] Espinosa S. and Catto P.J. 2017 *Plasma Phys. Control. Fusion* **59** 105001